

Preparation of Antibacterial, Arginine-Modified Ag Nanoclusters in the Hydrogel Used for Promoting Diabetic, Infected Wound Healing

Housen Jiang, Qin Xu, Xiaolin Wang, Lin Shi, Xuedong Yang, Jianmin Sun,* and Xifan Mei*

Cite This: *ACS Omega* 2023, 8, 12653–12663

Read Online

ACCESS |



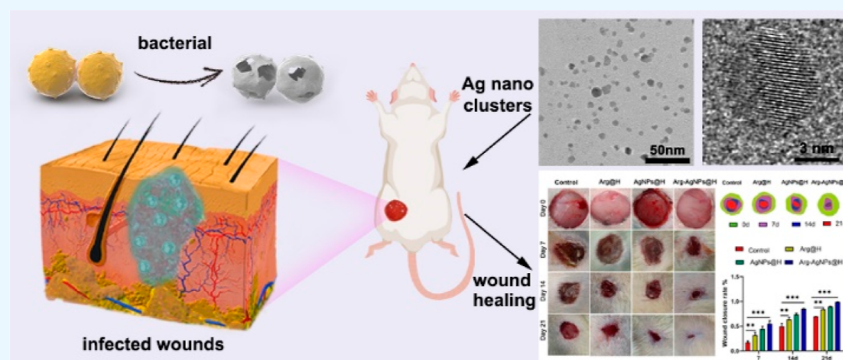
Metrics & More



Article Recommendations



Supporting Information



ABSTRACT: Diabetic foot ulcers with complex healing wounds accompanied by bacterial infection are considered a significant clinical problem which are made worse by the lack of effective treatments. Traditional antibiotics and dressings have failed to address wound infection and healing, and multifunctional combination therapies are attractive for treating chronic wounds. In this study, arginine (Arg) was loaded onto the surface of silver nanoclusters and encapsulated in a hydrogel to achieve antibacterial, anti-inflammatory, angiogenic, and collagen deposition functions through the slow release of Arg combined with silver nanoclusters. In vitro studies indicated that Arg-Ag@H composites inhibited methicillin-resistant *Staphylococcus aureus* and *Escherichia coli* by 94 and 97%, respectively. The inhibition of bacterial biofilms reached 85%, and the migration ability of human venous endothelial cells (HUVECs) increased by 50%. In vitro studies showed that Arg-Ag@H composites increased the healing area of wounds by 26% and resulted in a 98% skin wound-healing rate. Safety studies confirmed the excellent biocompatibility of Arg-Ag@H. The results suggest that Arg-Ag@H offers new possibilities for treating chronic diabetic wounds.

INTRODUCTION

Diabetic foot ulcers (DFUs) are one of the most severe chronic complications of diabetes and can lead to amputation in severe cases. According to the International Diabetes Federation in 2015, it is estimated that approximately 9.1–26.1 million people with diabetes develop foot ulcers each year.¹ Twenty percent of moderate to severe diabetic foot infections can result in varying degrees of amputation. Following amputation, the 5 year mortality rate for diabetic foot patients exceeds 70%.^{2,3} There is still a lack of effective treatment options for DFUs. Wound infections, especially drug-resistant bacterial and mixed infections, make diabetic wound healing a serious challenge.⁴ Clinical studies have shown that miscellaneous, mixed bacteria dominate diabetic trauma infections. Gram-positive bacteria (G^+) and Gram-negative bacteria (G^-) are the most common bacteria causing these infections, sometimes even accompanied by fungi.^{5–8} The application of antibiotics alone will not resolve the complex infection of the wound, and they are helpless in the repair of the wound. Exposed wounds and delayed healing can further lead to social and economic burdens and further impair patients' quality of

life. With the proper use and design of bioactive materials, the biological behavior of host cells can be effectively directed to promote tissue regeneration.^{9,10} It promotes a search for suitable topical multifunctional, anti-inflammatory, and antimicrobial dressings and acts as a matrix to promote wound healing.

Nanosilver ions are potent inhibitors or bactericides known for excellent antibacterial properties, capable of killing various pathogens and microorganisms such as bacteria, fungi, and viruses.^{11,12} They have long been widely used in medical and other products, including cosmetics, electronics, coatings, and disinfectants.¹³ The fundamental problem in applying Ag nanoclusters is the lack of stability and a tendency to aggregate.

Received: November 11, 2022

Accepted: March 7, 2023

Published: March 30, 2023



Once aggregated, it would lead to reduced antibacterial activity.¹⁴ Thus, a material that can both make the ions of Ag nanoclusters more uniformly distributed and protect them needs to be found. Of course, it would be better if the substance could also be directly or indirectly involved in the wound-healing process as a primary substance.¹⁵ Arginine has been used as a gene, protein, drug delivery agent, or a typical bioactive agent for wound healing due to its specific biological activity. Arginine is an essential amino acid. Its antibacterial effect is mainly due to its cationic nature, which can destroy the lipid bilayer of bacteria or the bacterial cell wall.¹⁶ In living organisms, arginine is involved in synthesizing peptides, thus promoting wound healing.¹⁷ Arginine is the only substitute for nitric oxide (NO) secretion, which plays a central role in antimicrobial action and regulation of vascular homeostasis.¹⁸ In addition, arginine is essential for synthesizing urea, polyamines, and creatine phosphate, all of which are necessary for chronic wound healing.¹⁹ Arginine meets our requirements and is an auspicious material. Therefore, we envisioned that the combination of arginine with Ag and the electrostatic repulsion of its cations would result in a more uniform distribution of Ag. They synergize with each other to produce a better bactericidal effect of Ag on the one hand. On the other hand, arginine itself is indispensable for wound healing. Its direct participation in wound healing can promote wound vascular formation, collagen precipitation, and tissue remodeling.

Sodium alginate is used as a thickener, stabilizer, and emulsifier under mild conditions for gel formation, which avoids the inactivation of active substances such as sensitive drugs, proteins, cells, and enzymes.²⁰ Sodium alginate hydrogels are used as carriers of arginine and Ag nanoclusters, which can fully and effectively exert antibacterial and wound-healing effects. Therefore, we developed a novel wound dressing by loading L-arginine and Ag nanoclusters into a hydrogel to investigate its possible role and mechanism in wound healing at the cellular level and in animal experiments.

2. MATERIALS AND METHODS

2.1. Preparation of Materials and Hydrogel Preparation. L-Arginine and sodium alginate were purchased from Aladdin Reagent (Shanghai) Co., Ltd. Methicillin-resistant *Staphylococcus aureus* (MRSA) and Gram-negative bacteria *Escherichia coli* (*E. coli*) were purchased from Guangdong Microbial Culture Collection (China). Dulbecco's modified Eagle's medium (DMEM), 3-(4,5-dimethylthiazol-2-yl)-2,5-diphenyl tetrazolium bromide (MTT), and fetal bovine serum (FBS) were purchased from Gibco (USA). The primary antibodies to CD31, vascular endothelial growth factor (VEGF), tubulin, and glyceraldehyde-3-phosphate dehydrogenase (GAPDH) were obtained from Cell Signaling Technology (USA). We used deionized water throughout the experiment. Polyvinyl alcohol (PVA) and sodium alginate (Alg) were provided by Sigma Chemical Co. (St. Louis, MO, USA).

2.2. Characterization of the Materials. The morphology of arginine-loaded silver nanoparticles was analyzed by transmission electron microscopy (TEM, JEM-1200EX, Japan). The size of arginine-loaded silver nanoparticles was characterized by dynamic laser scattering (DLS, Malvern, UK). The composition of arginine-loaded silver nanoparticles was detected by powder X-ray diffraction (XRD, Shimadzu, Kyoto, Japan).

2.3. Plate Counting Assay. After activation and incubation, MRSA and *E. coli* were incubated in fresh liquid LuriaBertani medium at 37 °C and treated with Arg-Ag@H or other nanomaterials before MRSA and *E. coli* (1.0×10^8 cfu/mL) were applied to agar plates. After 24 h incubation, bacteria were counted from each group and statistically analyzed. In addition, to further observe the antibacterial effect of the different material groups, treated *S. aureus* were fixed in 2.5% glutaraldehyde overnight at 4 °C. The morphology of the bacteria was observed by scanning electron microscopy (SEM).

2.4. Biofilm Formation Experiments. The biofilm model was used to assess the antibacterial membrane capacity of Arg-Ag@H. 2 mL of 5×10^8 cfu/mL bacteria was inoculated into 24-well plates and incubated for 48 h to establish biofilms. After different treatments, the effectiveness of the antibacterial film was evaluated by crystalline violet (CV) staining. Biofilms were washed with mild deionized water to remove the unbound dye. The bound CV was dissolved using absolute ethanol. Finally, the absorbance of all samples was measured by the enzyme marker at 590 nm.

2.5. Scratching Experiment. 5×10^5 HUVECs were inoculated into a 6-well plate. After the cells had spread evenly over the wells of the plate, a pipette tip was used to score in a straight line. After scratching, phosphate-buffered saline (PBS) wash was done 3 times to clean the scratched cells and replaced with serum-free medium. PBS was added as a blank control, and Arg@H, Ag@H, and Arg-Ag@H were co-cultured with the cells and placed in an incubator for 24 h. Then, the cells were washed with PBS and fixed with paraformaldehyde (PFA) for 30 min. 0.3% Triton X-100 was punched for 15 min and stained with DAPI. Pictures were taken under a fluorescence microscope, and the difference between the scratch wounds at 0, 6, and 12 h was calculated.

2.6. Cell Activity and Proliferative Capacity Assay. HUVECs were implanted in 96-well plates and incubated at 37 °C in a 5% CO₂ incubator for 24 h. In order to better mimic the microenvironment of bacterial infections in vivo, the cells were pretreated with 1 μg/mL lipopolysaccharide (LPS) followed by different nanomaterial treatments for 24 h. Cells treated with LPS alone were used as a positive control. The other treatments are as follows: first thiazole blue (0.5% MTT) was added to the pretreated cells and incubated for 4 h; then, 150 μL of dimethyl sulfoxide (DMSO) was added and shaken at a low speed for 15 min. Finally, quantitative detection was performed on a microplate reader at 490 nm.

2.7. Reactive Oxygen Experiment for HUVECs. HUVECs of the logarithmic growth phase were taken and seeded uniformly at 1×10^5 density in 6-well plates and cultured overnight. The next day, the cells were pretreated with different nanomaterials, and the culture was continued for 24 h each. Prepared DCFH-DA was added to each well, and with protection from light incubation was continued for 30 min. Intracellular reactive oxygen species (ROS) levels were observed using a fluorescence microscope and photographed. The fluorescence concentration of the images was quantified using the Image J software.

2.8. Immunofluorescence Assay. HUVECs were inoculated into small dishes or 24-well plates, treated with different material groups, incubated for 24 h, and then treated with 4% PFA for 40 min. Subsequently, 0.1% Triton X-100 was added and incubated for 15 min, followed by 5% goat serum for 2 h. Cells were incubated with primary antibodies CD31 (1:500,

Abcam, UK) and VEGF (1:500, Abcam, UK) overnight at 4 °C. Subsequently, incubation with secondary antibodies was performed for 2 h. Nuclei were stained with DAPI for 15 min; after washing, they were moistened with PBS, and with protection from light confocal laser scanning microscopy was performed to visualize the characteristics of the cells.

2.9. Diabetic Rat Model Preparation. The experiments were approved by the Experimental Animal Ethics Committee of Jinzhou Medical University (no. 20210094). Healthy male Sprague–Dawley rats, weighing between 180 and 200 g, were housed under standardized conditions. After being fed with high-fat and high-sugar diets for 1 month, the rats were injected intraperitoneally with 40 mg/kg streptozotocin (STZ) for 3 consecutive days. 72 h later, blood glucose levels >16.8 mmol/L were considered as successful modeling. Forty eligible rats were selected for subsequent animal experiments and then anesthetized intraperitoneally with 40 mg/kg pentobarbital sodium. A 1.5 × 1.5 cm full-thickness open excision wound was surgically created in the lateral dorsal region of the rats. The wound was injected with 100 μL of bacterial suspension to build an experimental infection model. The rats were divided into four groups and treated in different ways.

2.10. Wound-Healing Rate. The prepared Arg@H, Ag@H, and Arg-Ag@H hydrogels were applied directly to the wound site once on the same day after surgery and injected every 3 days. Subsequently, the trauma area, trauma healing, and epithelialization were observed daily. Photographs were taken on the first day and 7, 14, and 21 d postoperatively at the same fixed height, and digital photographs of each group of wounds were taken to quantify the wound-healing rate using ImageJ. Wound-healing rate (%) = (initial wound area – current wound area)/initial wound area × 100%. We then detected the expression levels of different inflammatory factors by ELISA kits.

2.11. Hematoxylin–Eosin Staining. Tissue preparation fragments (1.5 × 1.5 cm) of dorsal tissue from traumatic scars containing surrounding normal tissue were taken and fixed in neutral buffered formalin for 6 h, embedded in paraffin by conventional techniques, and sectioned to 5 μm thickness. The sections were stained with hematoxylin–eosin (H&E). The groups were observed for neutrophil and polymorphonuclear cell infiltration, fibroblasts, blood vessels, and collagen deposition under the dermis.

2.12. Masson Trichrome Staining. The sections were routinely dewaxed by water, Weigert ironwood stained for 5 min, acidic ethanol fractionated for 5–15 s, washed with water, and Masson blue wax solution returned to blue for 3 min. Using lixin red-magenta staining solution, drip staining was done for 3 min, and distilled water was used for rinsing slightly. After a weak acid solution treatment, phosphor aluminic acid solution wash was done for 1–2 min followed by aniline blue staining for 30 s. 95% ethanol, anhydrous ethanol dehydration, fast dehydration, xylene transparent, neutral gum sealing film, microscopic observation.

2.13. Immunohistochemistry. Paraffin sections were dewaxed and hydrated to extract the antigen required to detect CD31-positive cells. Endogenous peroxidase was blocked using an antibody diluent (Dako, S2022) and normal goat serum (Dako, Glostrup, Denmark). Tissue sections were then incubated overnight with primary antibody CD31 (PECAM1, Dako) and then incubated with secondary antibody. Sections were decolorized, hematoxylin re-stained, and day 21 sarcomeres were analyzed for vessel density. To

quantify CD31-positive vessels, five images were obtained from three tissue sections and analyzed using the ImageJ IHC profiler.

2.14. Statistical Analysis. All independent experiments were performed in triplicate in the corresponding condition. GraphPad Prism version 7 was applied for statistical analysis and statistical significance analysis using one-way variance analysis (ANOVA) with Tukey's post hoc test. Differences between groups at **P* < 0.05, ***P* < 0.01, and ****P* < 0.001 were considered statistically significant.

3. RESULTS AND DISCUSSION

3.1. Characteristics of the Material. Silver nanoparticles were first prepared by a stepwise growth method. Briefly, they were prepared by heating sodium citrate and deionized water, then boiling and adding silver nitrate and sodium borohydride. The above steps were repeated to obtain silver nanoparticles by stirring well under heated conditions and then adding silver nitrate and sodium borohydride. 0.8 g of PVA was dissolved in 10 mL of distilled water, 0.1 g of sodium alginate powder was added after PVA was completely dissolved, the temperature was raised to 70 °C, and the solution was mixed for 1 h with a magnetic field stirrer. The obtained silver nanoparticles were mixed with the hydrogel evenly to obtain the composite hydrogel. The synthesized arginine-loaded silver nanoclusters were characterized by TEM (Figure 1A). It can be seen that

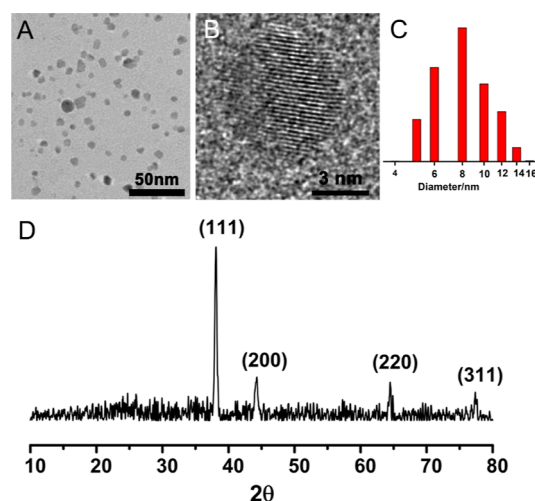


Figure 1. (A) TEM image of arginine-loaded silver nanoclusters. (B) Magnified image of high-resolution TEM of arginine-loaded silver nanoclusters. (C) DLS size distribution of the composite nanomaterials. (D) XRD patterns of the samples.

the particles of silver nanoclusters after loading arginine are uniform and have a good and stable dispersity. The lattice image of silver nanoclusters is clearly shown in the locally enlarged view in Figure 1B. The results of subsequent DLS showed that the size distribution of the composite silver nanoclusters was about 8 nm (Figure 1C). Finally, we confirmed by XRD that the diffraction peaks of the composite silver nanoclusters are located at 38.1, 44.2, 64.5, and 77.5°, which are consistent with the diffraction peaks of silver nanoclusters (Figure 1D). The above experimental results prove the successful preparation of the nanomaterials.

Considering the photothermal properties of silver nanoparticles, we further measured the photothermal effect of Arg-

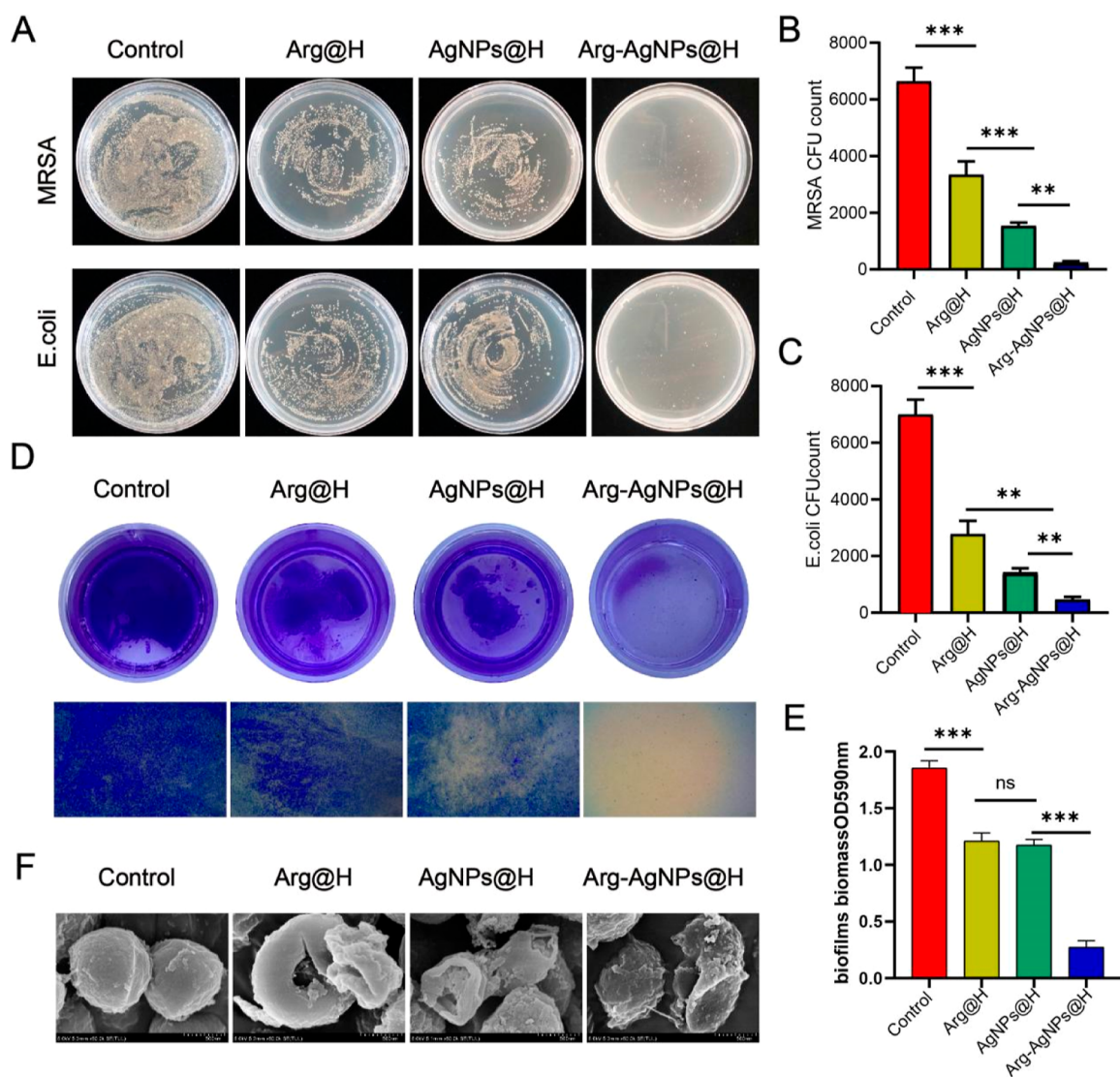


Figure 2. Antibacterial effect of different materials against *MRSA* and *E. coli*. (A) Bacterial colonization. (B) *MRSA* colonies on agar plates were calculated and statistically analyzed for the different treatment groups. (C) *E. coli* colonies on agar plates were calculated and statistically analyzed for the different treatment groups. (D) CV-stained biofilms and images of biofilms stained with crystal violet, bar = 200 μm . (E) Consequential statistics of histograms of biofilms; biomass OD 590 nm. (F) SEM images, bar = 500 μm . * $P < 0.05$, ** $P < 0.01$, *** $P < 0.001$.

AgNPs@H. The results showed a uniform temperature distribution without localized elevation, demonstrating the homogeneous distribution of the silver nanoclusters (Figure S1). We then examined the characteristic peaks of Ag nanoparticles by UV spectroscopy. The intensity of the characteristic peaks in the composite gel system was subsequently detected at different periods. The experimental results show that silver nanoparticles can be effectively released in the composite hydrogel system (Figure S2). In addition, the results of injectability experiments showed that the prepared hydrogel could be injected to exert specific adhesive effects on the wound, thus better acting as an antibacterial agent and promoting wound repair (Figure S3).

3.2. Antibacterial Experiments In Vitro. After analyzing the morphology and composition characterization, we tested the antibacterial properties of the composite nanoparticles. The bacteria colony counting experiment investigated the antibacterial effect of different hydrogel materials incubated for 24 h. The bactericidal rate of Arg-AgNPs@H for *MRSA* was 94% (Figure 2B), and the bactericidal rate of *E. coli* was 97%

(Figure 2C), both of which were significantly higher than in the control, Arg@H, and AgNPs@H groups. These results indicate that Arg-AgNPs@H can effectively inhibit the attachment and proliferation of bacteria and can effectively eliminate bacteria from infected wounds with a good antibacterial effect.

The CV staining assay was used to assess the ability of the Arg-AgNPs@H material to inhibit bacterial biofilm formation. After 6 h of incubation, the largest biofilm area was formed in the blank control group, and the smallest bacterial biofilm area was formed in the Arg-AgNPs@H-treated group (Figure 3D). Analysis of the absorbance of the biofilm (Figure 2E) showed that the inhibitory effect of AgNPs@H on biofilm formation was slightly stronger than that of Arg@H but still weaker than that of Arg-AgNPs@H, indicating that Arg-AgNPs@H has good antibacterial performance and good inhibition of bacterial biofilm formation (Figure 2D). To further evaluate the antibacterial and bacterial inhibitory effects of the materials, SEM was used to observe the cell morphological changes in *MRSA* after treatment with different materials. SEM

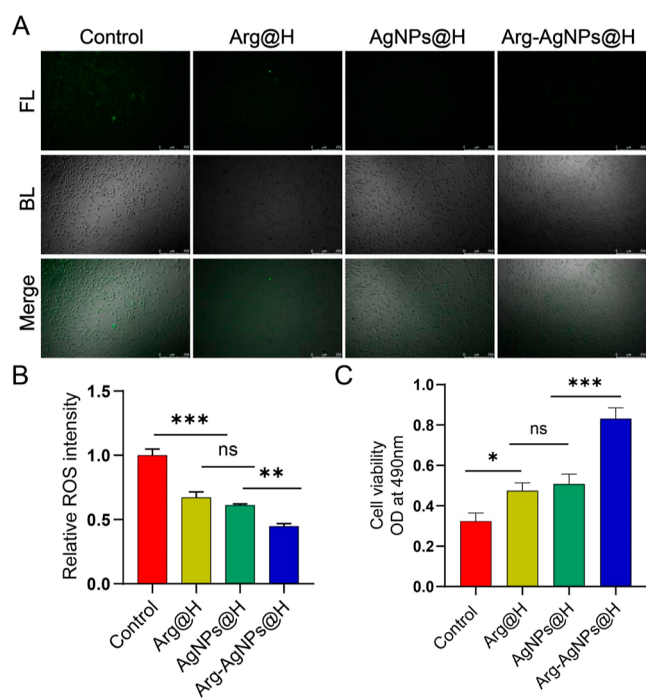


Figure 3. (A) Fluorescence images of ROS levels in HUVEC cells after incubation with different treatments. (B) Corresponding statistical histogram showing the relative ROS levels. (C) Corresponding statistical histogram of MTT analysis in different groups. * $P < 0.05$, ** $P < 0.01$, *** $P < 0.001$.

micrographs showed that the morphology of bacterial cells in the normal control group was typically spherical with a smooth surface. After Arg@H and AgNPs@H treatments, the bacterial cell morphology was locally disrupted, swollen, ruptured, and collapsed. In contrast, the structural distortion and destructive damage of bacteria after Arg-AgNPs@H treatment were more serious, leading to completely distorted and deformed morphology, large collapse, and lysis (Figure 2F). It indicates that Arg-AgNPs@H has a strong antibacterial effect and can kill bacteria by denaturing the enzymes in the bacterial cells and destroying the integrity of the cell membrane.

3.3. Materials Promote Cell Migration, Proliferation, and Endothelial Cell Angiogenesis and Reduce Redox Reactions.

The ROS fluorescent probe DCFH-DA was applied to assess the intracellular ROS levels in HUVECs and observe the materials' effect on cells. Relative to those of the LPS controls, Arg@H, AgNPs@H, and Arg-AgNPs@H fluorescence signals were significantly reduced, especially for Arg-AgNPs@H (Figure 3A). Analysis of their fluorescence signals revealed no significant difference in reactive oxygen fluorescence signals between Arg@H and AgNPs@H. At the same time, the Arg-AgNPs@H group had the lowest reactive oxygen fluorescence signal and reduced reactive oxygen levels by 55% relative to the LPS control group (Figure 3B). These results suggest that the novel nanomaterials can reduce the intracellular ROS generation in HUVECs and attenuate intracellular oxidative reduction damage, which has a protective effect. It was also demonstrated that the materials were well compatible with the cells, and no additional damage was caused.

To investigate whether Arg-AgNPs@H could safely coexist with HUVECs and induce their growth, we applied the MTT method to detect the proliferation ability of HUVECs further.

The results showed a significant difference in optical density (OD) values between the control and Arg@H groups and the AgNPs@H group. At the same time, there was no significant difference in OD values between the Arg@H group and the AgNPs@H group. Relative to the control group, the OD value of HUVECs in the Arg-AgNPs@H group was higher than twice that of the blank group (Figure 3C). It was shown that both Arg@H and AgNPs@H could promote proliferation, but the combination of both could promote the proliferation of HUVECs more effectively.

In order to investigate whether the new material Arg-AgNPs@H affects the migration ability of HUVECs, a scratch test was performed to verify it. After the scratch treatment, HUVECs gradually grew toward the scratch area. As shown in Figure 4A, the migration area after 6 h of treatment was

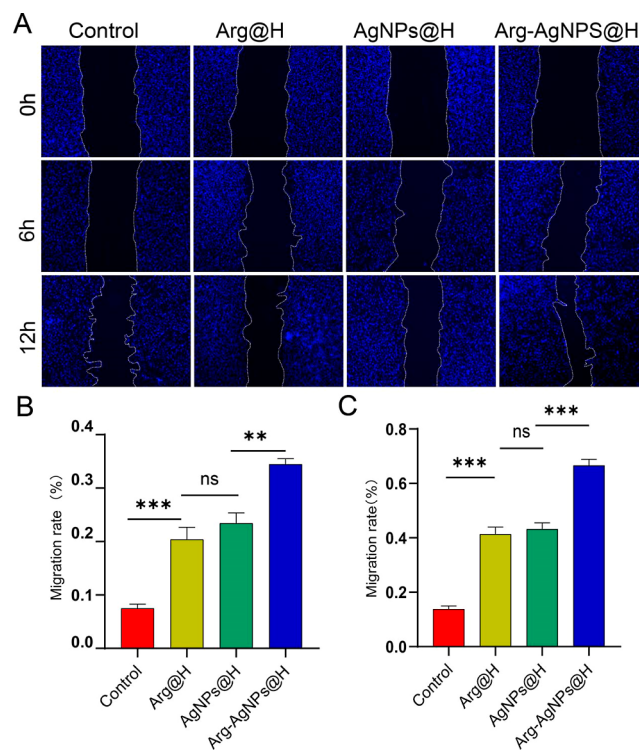


Figure 4. Promoting migration and proliferation effects and potential mechanism. (A) Digital images of scratch wound assay in different groups. (B) Quantification of HUVECs migration in 6 h. (C) Quantification of HUVECs migration in 12 h. * $P < 0.05$, ** $P < 0.01$, *** $P < 0.001$.

unchanged compared with the original scratch area in the control group. After treatment with different materials of Arg@H, AgNPs@H, and Arg-AgNPs@H, it could be observed that the cells migrated significantly. The blank area of the scratch was significantly reduced (Figure 4B). The migration of cells was more evident after 12 h of treatment. With the Arg-AgNPs@H group being the most obvious, the migration rate reached 54.3%, compared with 13% of the blank control group, the migration rate increased by 40%, and the difference was statistically significant (Figure 4C). These results fully indicate that Arg-AgNPs@H can significantly improve the migration ability of HUVECs.

Arg-AgNPs@H contributes to the regulation of the entire process of wound healing, and the nanosilver ions and arginine in hydrogel act through slow release. Various active factors of

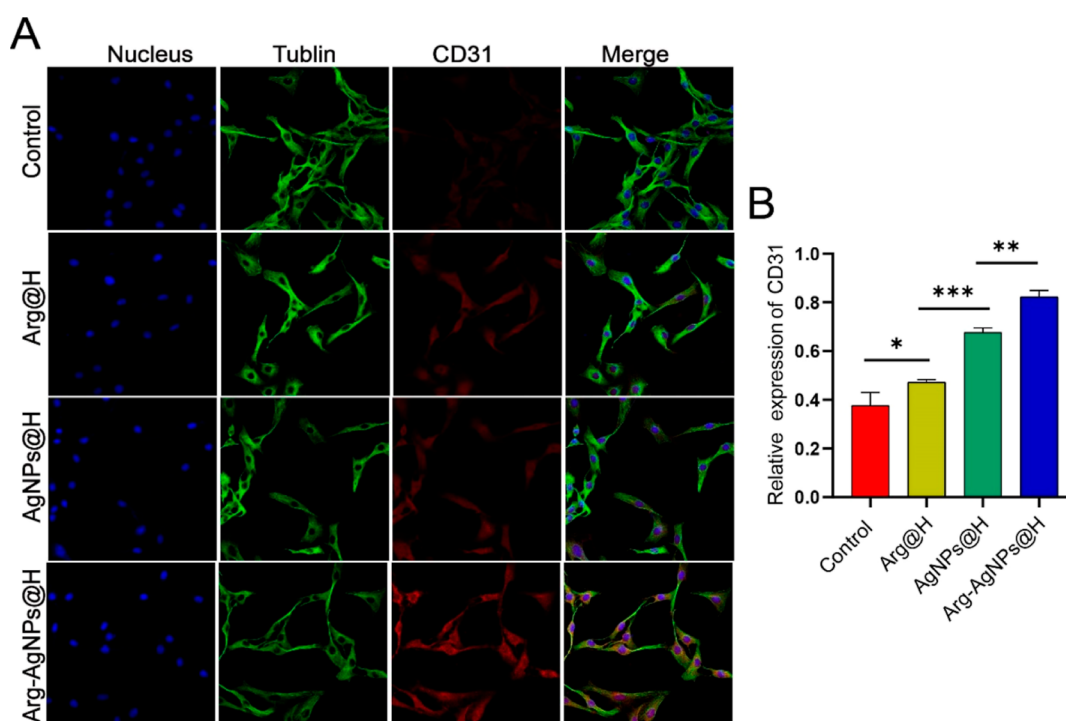


Figure 5. (A) CLSM images of the expression analysis of CD31, bar = 50 μm . (B) Semi-quantification analysis of CD31. * $P < 0.05$, ** $P < 0.01$, *** $P < 0.001$.

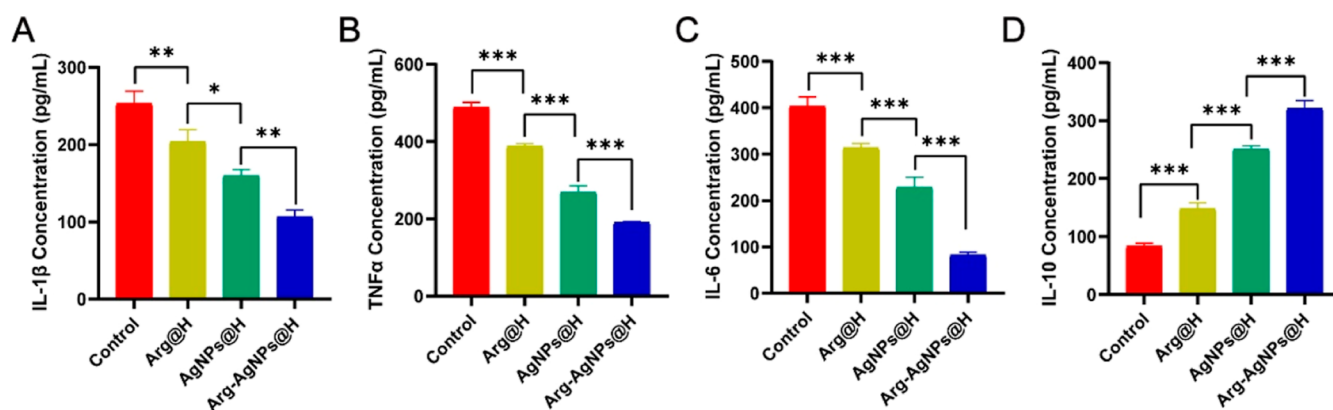


Figure 6. Level of the inflammatory factors (IL-1 β , TNF- α , IL-6) (A, B, and C) and anti-inflammatory factor (IL-10) (D) measured by ELISA kits. * $P < 0.05$, ** $P < 0.01$, *** $P < 0.001$.

arginine metabolism have been shown to trigger a complex set of physiological processes during the three phases of wound healing: hemostasis, inflammation, and proliferation, including collagen formation, cell proliferation, and immune regulation.²¹ To further confirm our inference, we performed confocal microscopy (CLSM) to detect the expression of relevant proteins. Numerous experimental studies have confirmed that CD31 and VEGF can assess the level of angiogenesis. High expression of CD31 indicates tightly connected vascular endothelial cells and involvement in neovascularization.²² During the inflammatory phase of diabetic wounds, defects such as tissue repair may be associated with diabetic wound angiogenesis. Activation of VEGF, a pro-angiogenic factor, leads to faster wound healing. We performed immunofluorescence experiments of CD31 and VEGF in cells to confirm this process and showed a slight improvement in CD31 expression by Arg@H. In contrast, AgNPs@H further improved the expression level of CD31

(Figure 5A), while the expression level of CD31 in the Arg-AgNPs@H group was significantly stronger than that in the Arg-AgNPs@H group. The results fully indicate the obvious pro-angiogenic effect of Arg-AgNPs@H (Figure 5B). Similarly, in the Arg-AgNPs@H treatment, the expression of VEGF was higher in the immunofluorescence assay (Figure S4A) than in all other groups. These results again demonstrated that Arg-AgNPs@H could promote CD31 and VEGF expression and promote angiogenesis to facilitate wound healing.

3.4. Assay of the Expression of Inflammatory Factors.

Oxidative stress activates multiple signaling pathways that lead to overexpression of chemokines, cell cycle regulatory molecules, and inflammatory cytokines.²³ Upregulation of the inflammatory response is the main reason for the prolonged wound closure time in diabetic patients. Inflammation plays a bidirectional role in regulating wound healing, and a certain level of inflammatory response can promote wound healing. However, an excessive inflammatory response can lead to a

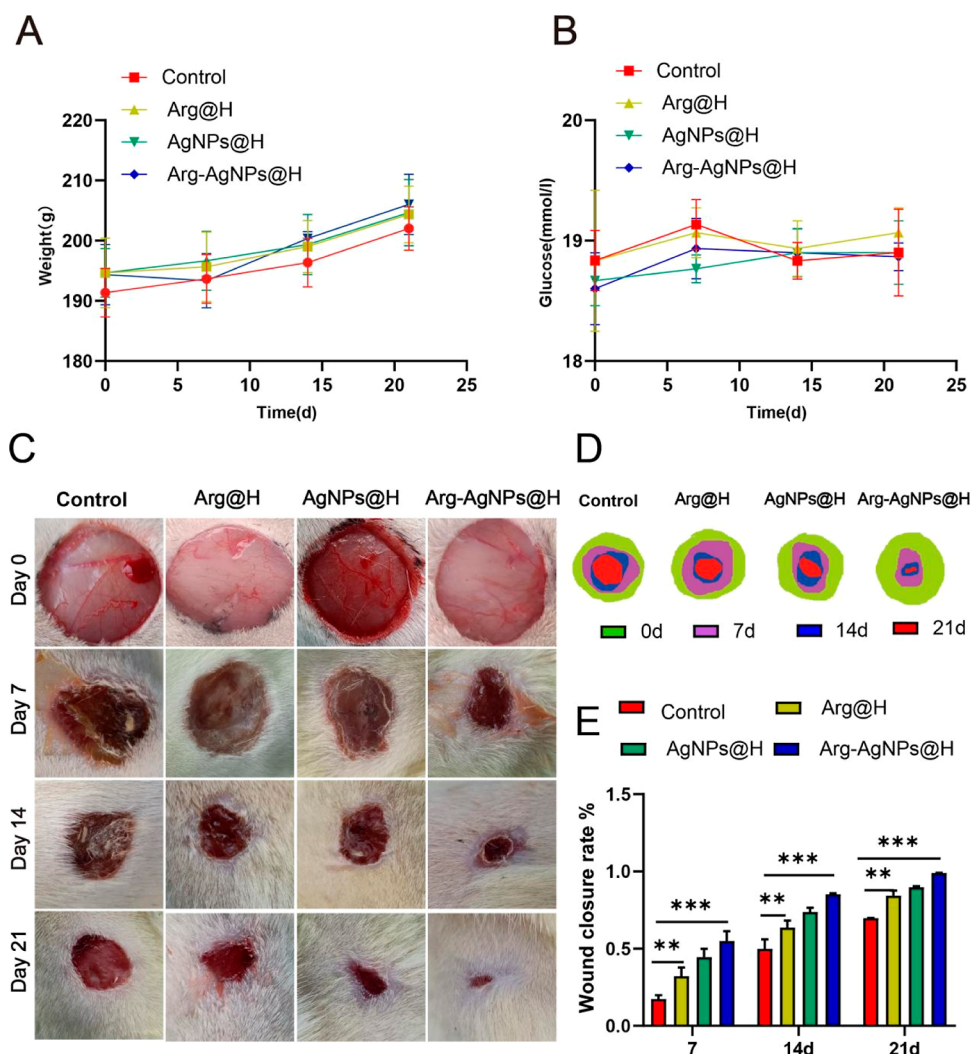


Figure 7. Evaluation effects of accelerating diabetic wounds in vivo. (A) Body weight curves of diabetic rats of different groups. (B) Blood glucose signatures of diabetic rats of different groups. (C) Images of diabetic wound healing at different times. (D) Traces of wound-bed closure during 21 days for each treatment. (E) Corresponding statistical graph of relative wound area from each group with different treatments. * $P < 0.05$, ** $P < 0.01$, *** $P < 0.001$.

long-term chronic inflammatory state that cannot be converted to a proliferative state.²⁴ During the inflammatory phase of wounds in either type 1 or type 2 diabetic patients, neutrophils and macrophages aggregate slowly, inflammatory factor expression is elevated at baseline, and macrophage phagocytosis is reduced.²⁵ The phagocytic capacity of leukocytes is impaired, inflammatory cytokines are present in diabetic wounds for much longer than normal, the inflammatory phase is prolonged, and granulation tissue formation is impaired.²⁶ Diabetic wounds exhibit high expression of pro-inflammatory factors IL-1 β , IL-6, and TNF- α and reduced expression of anti-inflammatory factor IL-10.^{27,28} When the wound releases anti-inflammatory factors instead of pro-inflammatory factors, the wound completes the transition from the inflammatory phase to the proliferative phase.^{29,30} In this experiment, by simulating the in vitro inflammatory environment, it was found that the level of pro-inflammatory factors significantly decreased and the level of anti-inflammatory factors significantly increased after treatment with the material, with the best effect in the Arg-AgNPs@H group, and the difference was statistically significant (Figure 6).

3.5. In Vivo Biological Assessment. Diabetic animal models were established using STZ. The changes of blood glucose and body weight of the experimental animals in each group were continuously observed, and the blood glucose of the animals in each group continuously fluctuated between 18.5 and 19.5 mmol/L, and the body weight continuously and slowly increased. Figure 7A shows the body weight change curve of the experimental animals, and Figure 7B shows the change of blood glucose.

Figure 7C shows broad photographs of the wounds of different groups of rats at specific time points after molding (days 0, 7, 14, and 21). Figure 7D shows the effect of wound healing superimposed on the data measured by ImageJ for each group, and Figure 7E shows the analysis of the healing rate for each group at each time point. The broad images show a significant decrease in wound area over time for each group, particularly on postoperative days 7 and 14. Compared to the control group, the Arg@H, AgNPs@H, and Arg-AgNPs@H groups showed a significant reduction in wound size, with Arg-AgNPs@H standing out, indicating that Arg-AgNPs@H allows for rapid wound healing. In addition, the wounds in the Arg-AgNPs@H group were significantly more minor than in the

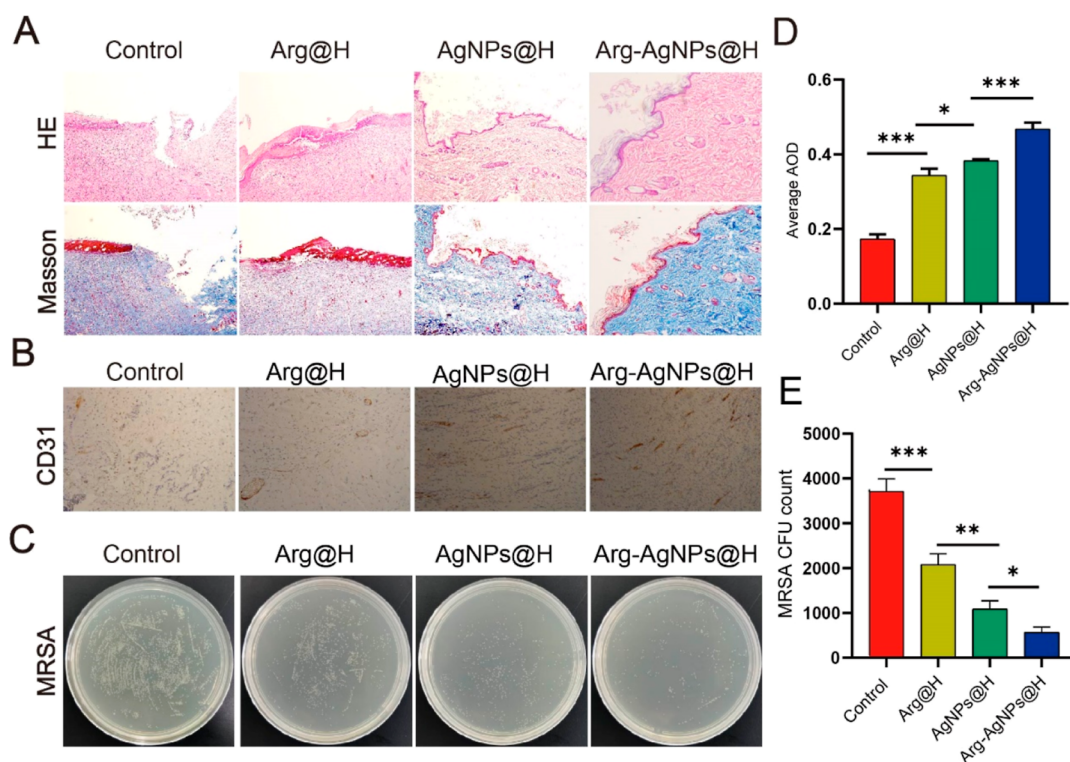


Figure 8. Evaluation on the healing-promoting effect of the nanoplateforms on wounds. (A) H&E and Masson staining of wound sites with different treatments. (B) IMHC staining of wound sites with different treatments. (C) Reduced MRSA colonization of diabetic wounds and inhibited inflammation. (D) Quantification analysis of CD31. (E) MRSA colonies were calculated and statistically analyzed for the different treatment groups. * $P < 0.05$, ** $P < 0.01$, *** $P < 0.001$.

Arg@H and AgNPs@H groups on postoperative days 7 and 14. On postoperative day 21, the wounds in the Arg-AgNPs@H group were almost repaired to a closed state, while the wounds in the blank group were still clearly visible. As can be seen from the bar graph, the average healing area of Arg-AgNPs@H was over 90% at day 21 postoperatively in both groups (Figure 7E). This improved healing rate was mainly attributed to the sustained local slow release of arginine and silver nanoparticles in the sodium alginate hydrogel. Arginine and silver nanoparticles play an essential role in multiple stages of wound healing by promoting HUVEC migration and proliferation, neovascularization, and collagen formation and maturation.

3.6. Tissue Staining and Immunohistochemistry. To further evaluate the wound healing, we took wound specimens 21 days after surgery to observe the histological changes in the wounds. We used H&E to observe the microstructure of the healing skin. Compared with the Arg@H, AgNPs@H, and Arg-AgNPs@H groups, the control group could not form complete epithelial tissue and local scab coverage, and there was interruption, rupture, buckling, and many inflammatory cells infiltrating and proliferating in the subcutaneous tissue and a small amount of collagen fiber precipitation. The Arg@H group had incomplete epithelialization, local scab covering the wound, more complete coverage, and a small amount of subcutaneous tissue inflammatory cell infiltration; the AgNPs@H and Arg-AgNPs@H groups had completed the process of re-epithelialization, and the epithelium of the Arg-AgNPs@H group was smoother and more regular than that of the AgNPs@H group. Hair follicle formation was visible around the wound (Figure 8A). We evaluated it using Masson staining to better show the precipitation and production of

collagen within the wound. Only a small number of collagen fiber bundles appeared in the control group. They were loosely organized, disorganized, and disordered. Compared with the control group, for the Arg@H, AgNPs@H, and Arg-AgNPs@H groups, many collagen fibers were visible at the wound and were arranged in an orderly manner. In contrast, the Arg-AgNPs@H group had a thicker morphology and a more regular arrangement of collagen fibers. These results suggest that Arg-AgNPs@H is more able to reduce the inflammatory response of wounds and promote the production and deposition of collagen in wounds.

To further assess the proliferation of blood vessels in experimental animal tissues, CD31 immunohistochemical staining was performed on skin tissues in this study. In immunohistochemical staining, CD31 is used to demonstrate the presence of vascular endothelial cells in tissues. The neovascularization number was significantly higher in the Arg@H, AgNPs@H, and Arg-AgNPs@H groups than in the blank control group, as seen microscopically (Figure 8B). Analysis of the average optical density (AOD) of CD31 expression was the highest in the Arg-AgNPs@H group, indicating that the amount of neovascularization in the Arg-AgNPs@H group was significantly much higher than in the other groups (Figure 8D). These results are highly consistent with CD31 immunofluorescence results in cellular assays, demonstrating that the novel material significantly promoted vascular proliferation in vivo and in vitro.

3.7. Materials Promote In Vivo Healing of MRSA Infections in Diabetic Wounds. The diabetic rat's model was established with STZ. Then the wounds were injected with 100 μL of (1.0×10^8 cfu/mL) MRSA to simulate a clinical diabetic wound infection model to study the antimicrobial

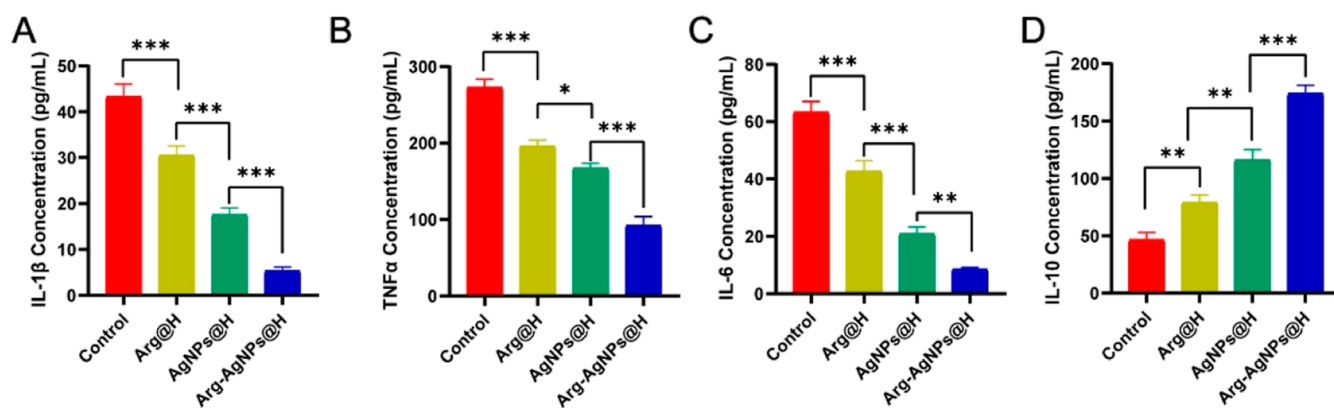


Figure 9. Levels of the inflammatory factors (IL-1 β , TNF- α , IL-6) (A,B, and C) and anti-inflammatory factor (IL-10) (D) measured by ELISA kits. * $P < 0.05$, ** $P < 0.01$, *** $P < 0.001$.

ability of our material. Wound samples from the animal model were taken 3 days after surgery, and extracts were tested for bacterial colony counts on agar plates. The antibacterial activity was further evaluated by comparing the bacterial cfu in the infected area. It was seen that the number of proliferating Arg-AgNPs@H MRSA colonies was significantly less than that of the blank control (Figure 8C), and the bactericidal rate was 85% (Figure 8E). Although it is lower than 94% in the in vitro experiment, it also indicates that the novel material can kill bacteria sufficiently and effectively on the traumatic surface with an excellent bactericidal effect, consistent with our evaluation of the in vitro antibacterial results.

3.8. Assays of Inflammatory Factors in Tissues. The in vitro results showed that Arg-AgNPs@H has the effect of reducing the release of inflammatory factors. We then collected samples at the wound sites to detect the expression of each inflammatory factor to verify the anti-inflammatory effect of Arg-AgNPs@H in vivo.

The expression of pro-inflammatory factors interleukin-1 (IL-1 β), interleukin 6 (IL-6), and tumor necrosis factor (TNF) was significantly lower in the Arg-AgNPs@H group compared to the control, Arg@H, and AgNPs@H groups (Figure 9A–C). Meanwhile, the expression of anti-inflammatory cytokines such as IL-10 was upregulated (Figure 9D). This demonstrates that Arg-AgNPs@H has the same advantage of attenuating the expression of pro-inflammatory factors and promoting the proliferation of anti-inflammatory factors in vitro. The trend of inflammatory factor expression in in vitro experiments is highly consistent with that of in vivo experiments.

3.9. Safety Experiments with the Material. The above in vitro results fully demonstrate that Arg-AgNPs@H has significant antibacterial, anti-inflammatory, and angiogenesis effects, significant wound-healing properties, and the potential to promote wound healing. However, as a novel material, the safety evaluation of the material in animal experiments is crucial to be promoted and applied in the clinical setting. Blood and organ sections from rats were analyzed to assess the biosafety of the nanomaterials. We performed a biochemical analysis of blood on day 21. Liver function indices (ALT, AST) and kidney function indices (BUN, CREA) in the Arg-AgNPs@H group were within the normal range (Figure S5). Meanwhile, for the Arg-AgNPs@H group, typical anatomical structures of each organ (heart, liver, spleen, lung, and kidney) were seen in H&E staining. No significant inflammation and necrosis were seen in the microscopic tissue structures (Figure S6). These results suggest that Arg-AgNPs@H can be used as a

safe and effective material to accelerate the healing of infected diabetic wounds.

4. CONCLUSIONS

Wound healing remains a major clinical challenge due to the deterioration of the tissue microenvironment, excessive inflammation, and bacterial infection.^{31,32} Management of wounds that are inherently difficult to heal due to diseases such as diabetes remains highly challenging in clinical practice.^{33,34} In addition, due to the loss of inherent skin protection, skin wounds can become more susceptible to bacterial infections and further prevent wound healing. Today, a variety of dressings have been developed for wound care.^{35,36} Traditional dressings such as gauze, cotton, and bandages do not provide a moist environment at the wound interface and do not prevent bacterial infection. Proper use of bioactive materials can provide the optimal structural and functional microenvironment for tissue reconstruction.^{37,38} For the healing of infected wounds, it is essential to effectively regulate the biological activity of the wound microenvironment and eliminate bacterial infection to promote wound healing.^{39,40} During this experiment, we developed Arg-AgNPs@H hydrogel by using sodium alginate hydrogel as a carrier and selecting nanosilver and arginine as matching materials in the antibacterial, anti-inflammatory, pro-vascular proliferation, and collagen precipitation. The hydrogel externally isolates the external environment from the wound, while internally, it provides an antiseptic, anti-inflammatory, and healing-promoting microenvironment. In addition, in vitro and in vivo studies showed that Arg-AgNPs@H hydrogels effectively inhibit bacterial proliferation and promote angiogenesis. In addition, the composite reduces the release of pro-inflammatory factors from the wound surface and ultimately promotes wound repair. In addition, the novel gel also promotes the proliferation and hyperplasia of HUVECs and promotes collagen deposition and vascular angiogenesis, thus accelerating diabetic wound healing. We expect that Arg-AgNPs@H hydrogel can be widely used as a reliable topical dressing in the future and play a more significant role in the healing of diabetic wounds and chronic wounds.

ETHICS APPROVAL

All animal studies were approved by the Institutional Ethics Committee of Jinzhou Medical University.

■ ASSOCIATED CONTENT

SI Supporting Information

The Supporting Information is available free of charge at <https://pubs.acs.org/doi/10.1021/acsomega.2c07266>.

Distribution of the silver nanoclusters; UV–vis absorbance of Ag nanoparticles; testing of hydrogel injectability; and expression analysis of VEGF (PDF)

■ AUTHOR INFORMATION

Corresponding Authors

Jianmin Sun – Department of Hand and Foot Orthopedic Surgery, Weifang People's Hospital, Weifang 261042, China; Email: sjmwxxy@163.com

Xifan Mei – Department of Orthopedics, Third Affiliated Hospital of Jinzhou Medical University, Jinzhou 121000, China; orcid.org/0000-0002-4452-8005; Email: meixifan1971@163.com

Authors

Housen Jiang – Dalian Medical University, Dalian 116044 Liaoning, China; Department of Hand and Foot Orthopedic Surgery, Weifang People's Hospital, Weifang 261042, China

Qin Xu – Department of Hand and Foot Orthopedic Surgery, Weifang People's Hospital, Weifang 261042, China

Xiaolin Wang – Department of Pathology, Weifang Hospital of Traditional Chinese Medicine, Weifang 261042, China

Lin Shi – Department of Hand and Foot Orthopedic Surgery, Weifang People's Hospital, Weifang 261042, China

Xuedong Yang – Department of Hand and Foot Orthopedic Surgery, Weifang People's Hospital, Weifang 261042, China

Complete contact information is available at:

<https://pubs.acs.org/doi/10.1021/acsomega.2c07266>

Author Contributions

Data curation and writing, H.J.; formal analysis, L.S. and X.Y.; methodology, Q.X. and X.W.; project administration, X.M. and J.S. All authors reviewed the manuscript.

Notes

The authors declare no competing financial interest.

■ ACKNOWLEDGMENTS

We would like to give our sincere gratitude to the reviewers for their constructive comments.

■ REFERENCES

- (1) Armstrong, D. G.; Boulton, A. J. M.; Bus, S. A. Diabetic foot ulcers and their recurrence. *N. Engl. J. Med.* **2017**, *376*, 2367–2375.
- (2) Lipsky, B. A.; Berendt, A. R.; Cornia, P. B.; Pile, J. C.; Peters, E. J.; Armstrong, D. G.; Deery, H. G.; Embil, J. M.; Joseph, W. S.; Karchmer, A. W.; et al. Infectious Diseases Society of America clinical practice guideline for the diagnosis and treatment of diabetic foot infections. *Clinical Infectious Diseases* **2012**, *54*, e132–e173.
- (3) Lavery, L. A.; Armstrong, D. G.; Wunderlich, R. P.; Tredwell, J.; Boulton, A. J. Diabetic foot syndrome: evaluating the prevalence and incidence of foot pathology in Mexican Americans and non-Hispanic whites from a diabetes disease management cohort. *Diabetes Care* **2003**, *26*, 1435–1438.
- (4) Lavery, L. A.; Hunt, N. A.; Ndip, A.; Lavery, D. C.; Van Houtum, W.; Boulton, A. J. Impact of chronic kidney disease on survival after amputation in individuals with diabetes. *Diabetes Care* **2010**, *33*, 2365–2369.

- (5) Mandla, S.; Davenport Huyer, L.; Radisic, M. Multimodal bioactive material approaches for wound healing. *APL Bioengineering* **2018**, *2*, 021503.

- (6) Jara, C. P.; Mendes, N. F.; Prado, T. P. D.; de Araújo, E. P. Bioactive fatty acids in the resolution of chronic inflammation in skin wounds. *Adv. in Wound Care* **2020**, *9*, 472–490.

- (7) Zhou, L.; Xi, Y.; Xue, Y.; Wang, M.; Liu, Y.; Guo, Y.; Lei, B. Injectable self-healing antibacterial bioactive polypeptide-based hybrid nanosystems for efficiently treating multidrug resistant infection, skin-tumor therapy, and enhancing wound healing. *Adv. Funct. Mater.* **2019**, *29*, 1806883.

- (8) Caihong, X.; Gu, Z.; Guiting, L.; Jun, W. Whole wheat flour coating with antioxidant property accelerates tissue remodeling for enhanced wound healing. *Chin. Chem. Lett.* **2020**, *31*, 1612–1615.

- (9) Zhou, Y.; Han, S.; Liang, Z.; Zhao, M.; Liu, G.; Wu, J. Progress in arginine-based gene delivery systems. *J. Mater. Chem. B* **2020**, *8*, 5564–5577.

- (10) Kim, H. S.; Sun, X.; Lee, J. H.; Kim, H. W.; Fu, X.; Leong, K. W. Advanced drug delivery systems and artificial skin grafts for skin wound healing. *Adv. Drug Delivery Rev.* **2019**, *146*, 209–239.

- (11) Witte, M. B.; Thornton, F. J.; Tantry, U.; Barbul, A. L-Arginine supplementation enhances diabetic wound healing: involvement of the nitric oxide synthase and arginase pathways. *Metabolism-Clinical and Experimental* **2002**, *51*, 1269–1273.

- (12) Meng, Z.; Zhou, D.; Gao, Y.; Zeng, M.; Wang, W. miRNA delivery for skin wound healing. *Adv. Drug Delivery Rev.* **2018**, *129*, 308–318.

- (13) Wu, G.; Bazer, F. W.; Davis, T. A.; Kim, S. W.; Li, P.; Marc Rhoads, J.; Carey Satterfield, M.; Smith, S. B.; Spencer, T. E.; Yin, Y. Arginine metabolism and nutrition in growth, health, and disease. *Amino Acids* **2009**, *37*, 153–168.

- (14) You, X.; Gu, Z.; Huang, J.; Kang, Y.; Chu, C. C.; Wu, J. Arginine-based poly (ester amide) nanoparticle platform: From structure–property relationship to nucleic acid delivery. *Acta Biomater.* **2018**, *74*, 180–191.

- (15) Zhang, X.; Duan, Y.; Wang, D.; Bian, F. Preparation of arginine modified PEI-conjugated chitosan copolymer for DNA delivery. *Carbohydr. Polym.* **2015**, *122*, 53–59.

- (16) Liu, G.; Bao, Z.; Wu, J. Injectable baicalin/F127 hydrogel with antioxidant activity for enhanced wound healing. *Chin. Chem. Lett.* **2020**, *31*, 1817–1821.

- (17) Wu, M.; Lu, Z.; Wu, K.; Nam, C.; Zhang, L.; Guo, J. Recent advances in the development of nitric oxide-releasing biomaterials and their application potentials in chronic wound healing. *J. Mater. Chem. B* **2021**, *9*, 7063–7075.

- (18) Han, G.; Nguyen, L. N.; Macherla, C.; Chi, Y.; Friedman, J. M.; Nosanchuk, J. D.; Martinez, L. R. Nitric oxide–releasing nanoparticles accelerate wound healing by promoting fibroblast migration and collagen deposition. *Am. J. Pathol.* **2012**, *180*, 1465–1473.

- (19) Durante, W.; Johnson, F. K.; Johnson, R. A. Arginase: a critical regulator of nitric oxide synthesis and vascular function. *Clinical and Experimental Pharmacology & Physiology* **2007**, *34*, 906.

- (20) Mi, G.; Shi, D.; Herchek, W.; Webster, T. J. Self-assembled arginine-rich peptides as effective antimicrobial agents. *Journal of Biomedical Materials Research Part A* **2017**, *105*, 1046–1054.

- (21) Zeng, Q.; Qi, X.; Shi, G.; Zhang, M.; Haick, H. Wound Dressing: From Nanomaterials to Diagnostic Dressings and Healing Evaluations. *ACS Nano* **2022**, *16*, 1708–1733.

- (22) He, W.; Zhang, F.; Fan, Z. Application of nano-silver antibacterial technology in clinical healthcare. *Chinese Journal of Tissue Engineering Research* **2010**, *14*, 7899.

- (23) Rustogi, R.; Mill, J.; Fraser, J. F.; Kimble, R. M. The use of Acticoat in neonatal burns. *Burns* **2005**, *31*, 878–882.

- (24) Silver, S.; Phung, L. T. A bacterial view of the periodic table: genes and proteins for toxic inorganic ions. *Journal of Industrial Microbiology and Biotechnology* **2005**, *32*, 587–605.

- (25) Ruszczak, Z. Effect of collagen matrices on dermal wound healing. *Adv. Drug Delivery Rev.* **2003**, *55*, 1595–1611.

(26) Wittmann, F.; Prix, N.; Mayr, S.; Angele, P.; Wichmann, M. W.; van den Engel, N. K.; Hernandez-Richter, T.; Chaudry, I. H.; Jauch, K. W.; Angele, M. K. L-arginine improves wound healing after trauma-hemorrhage by increasing collagen synthesis. *J Trauma* **2005**, *59*, 162–168.

(27) Wang, C.; Liang, C.; Wang, R.; Yao, X.; Guo, P.; Yuan, W.; Liu, Y.; Song, Y.; Li, Z.; Xie, X. The fabrication of a highly efficient self-healing hydrogel from natural biopolymers loaded with exosomes for the synergistic promotion of severe wound healing. *Biomater. Sci.* **2020**, *8*, 313–324.

(28) Reuter, S.; Gupta, S. C.; Chaturvedi, M. M.; Aggarwal, B. B. Oxidative stress, inflammation, and cancer: how are they linked? *Free radical Biology and Medicine* **2010**, *49*, 1603–1616.

(29) Boniakowski, A. E.; Kimball, A. S.; Jacobs, B. N.; Kunkel, S. L.; Gallagher, K. A. Macrophage-mediated inflammation in normal and diabetic wound healing. *The Journal of Immunology* **2017**, *199*, 17–24.

(30) Gustinelli Barbosa, M. A.; Paggiaro, A. O.; Carvalho, V.; Isaac, C.; Gemperli, R. Effects of hydrogel with enriched sodium alginate in wounds of diabetic patients. *Plastic Surgical Nursing* **2018**, *38*, 133–138.

(31) Liu, W.; Gao, R.; Yang, C.; Feng, Z.; Ou-Yang, W.; Pan, X.; Huang, P.; Zhang, C.; Kong, D.; Wang, W. ECM-mimetic immunomodulatory hydrogel for methicillin-resistant *Staphylococcus aureus*-infected chronic skin wound healing. *Sci. Adv.* **2022**, *8*, No. eabn7006.

(32) Dong, R.; Guo, B. Smart wound dressings for wound healing. *Nano Today* **2021**, *41*, 101290.

(33) Choi, H.; Kim, B.; Jeong, S. H.; Kim, T. Y.; Kim, D. P.; Oh, Y. K.; Hahn, S. K. Microalgae-Based Biohybrid Microrobot for Accelerated Diabetic Wound Healing. *Small* **2022**, *19*, 2204617.

(34) Kong, C.; Chen, S.; Ge, W.; Zhao, Y.; Xu, X.; Wang, S.; Zhang, J. Riclin-Capped Silver Nanoparticles as an Antibacterial and Anti-Inflammatory Wound Dressing. *Int. J. Nanomed.* **2022**, *17*, 2629–2641.

(35) Dong, R.; Li, Y.; Chen, M.; Xiao, P.; Wu, Y.; Zhou, K.; Zhao, Z.; Tang, B. Z. In Situ Electrospinning of Aggregation-Induced Emission Nanofibrous Dressing for Wound Healing. *Small Methods* **2022**, *6*, 2101247.

(36) Boniakowski, A. M.; denDekker, A. D.; Davis, F. M.; Joshi, A.; Kimball, A. S.; Schaller, M.; Allen, R.; Bermick, J.; Nycz, D.; Skinner, M. E.; et al. SIRT3 regulates macrophage-mediated inflammation in diabetic wound repair. *J. Invest. Dermatol.* **2019**, *139*, 2528–2537.

(37) Liu, D.; Yang, P.; Gao, M.; Yu, T.; Shi, Y.; Zhang, M.; Yao, M.; Liu, Y.; Zhang, X. NLRP3 activation induced by neutrophil extracellular traps sustains inflammatory response in the diabetic wound. *Clin. Sci.* **2019**, *133*, 565–582.

(38) Mirza, R. E.; Fang, M. M.; Weinheimer-Haus, E. M.; Ennis, W. J.; Koh, T. J. Sustained inflammasome activity in macrophages impairs wound healing in type 2 diabetic humans and mice. *Diabetes* **2014**, *63*, 1103–1114.

(39) Finley, P. J.; DeClue, C. E.; Sell, S. A.; DeBartolo, J. M.; Shornick, L. P. Diabetic wounds exhibit decreased Ym1 and arginase expression with increased expression of IL-17 and IL-20. *Advances in Wound Care* **2016**, *5*, 486–494.

(40) Parisi, L.; Gini, E.; Baci, D.; Tremolati, M.; Fanuli, M.; Bassani, B.; Farronato, G.; Bruno, A.; Mortara, L. Macrophage polarization in chronic inflammatory diseases: killers or builders. *J. Immunol. Res.* **2018**, *2018*, 1–25.